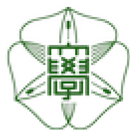

HOKKAIDO UNIVERSITY

Title	Anisotropic defect distribution in He+-irradiated 4H-SiC: Effect of stress on defect distribution
Author(s)	Yang, Subing; Nakagawa, Yuki; Kondo, Minako; Shibayama, Tamaki
Citation	Acta materialia, 211, 116845 https://doi.org/10.1016/j.actamat.2021.116845
Issue Date	2021-06-01
Doc URL	http://hdl.handle.net/2115/88735
Rights	© <2021>. This manuscript version is made available under the CC-BY-NC-ND 4.0 license http://creativecommons.org/licenses/by-nc-nd/4.0/
Rights(URL)	http://creativecommons.org/licenses/by-nc-nd/4.0/
Type	article (author version)
File Information	Manuscript_revised-unmarked.pdf

Instructions for use

Hokkaido University Collection of Scholarly and Academic Papers : HUSCAP

Anisotropic defect distribution in He^{+}-irradiated 4H-SiC: effect of stress on defect distribution

Subing Yang, Yuki Nakagawa, Minako Kondo, Tamaki Shibayama*
Faculty of Engineering, Hokkaido University, Sapporo, Hokkaido 060-8628, Japan
* Corresponding author.
E-mail address: shiba@qe.eng.hokudai.ac.jp

22 **Abstract**

23 Irradiation-induced anisotropic swelling in hexagonal α-SiC is known to
24 degrade the mechanical properties of SiC; however, the associated physical
25 mechanism and microstructural process remain insufficiently understood.
26 In this study, an anisotropic swelling condition where the surface normal
27 direction was allowed to freely expand with constraint in the lateral
28 direction was introduced in 4H-SiC using selected-area He^+ irradiation, and
29 the internal defect distribution was investigated using transmission electron
30 microscopy (TEM) and advanced scanning TEM. The defect distribution
31 was compared to that in non-selected-area He^+-irradiated 4H-SiC and
32 electron-irradiated TEM-foil 4H-SiC. An anisotropic defect distribution
33 was observed in the selected-area He^+-ion-irradiated 4H-SiC, with
34 interstitial defects preferentially redistributed in the surface normal
35 direction ([0004]) and negative volume defects (such as vacancies and/or
36 carbon antisite defects) dominantly located in the lateral directions ($[11\bar{2}0]$
37 and $[10\bar{1}0]$). This anisotropy of the defect distribution was substantially
38 lower in the non-selected-area He^+-irradiated and electron-irradiated
39 samples. The stress condition in the three samples was also measured and
40 analyzed. In the selected-area He^+-irradiated 4H-SiC, compressive stress
41 was introduced in the lateral directions (($[10\bar{1}0]$ and $[11\bar{2}0]$)), with little
42 stress introduced in the surface normal direction ([0004]); this stress
43 condition was introduced at the beginning of ion irradiation. The
44 compressive stress likely inhibits the formation of interstitial defects in the
45 lateral directions, enhancing the anisotropy of the defect distribution in

46 SiC.

47 **Keywords:** Silicon carbide; Irradiation effect; Swelling; Defects; TEM.

48 1. Introduction

49 Because of its excellent mechanical, structural, and electronic properties,
50 silicon carbide (SiC) has been proposed as an excellent candidate for
51 various nuclear, aerospace, and electronic applications [1-4]. SiC is
52 exposed to various types of irradiation during the fabrication of electronic
53 devices (such as ion implantation for doping carriers) or when applied in
54 nuclear or aerospace environments (neutron or other high-energy particle
55 irradiations) [5-6]. This irradiation inevitably introduces damage, which
56 greatly affects the mechanical and electronic properties. Particular interest
57 has been focused on irradiation-induced dimension instability, including
58 swelling [7] and creeping [8], which is a key issue for long-term structural
59 performance in nuclear reactors. In order to resolve these issues, one of the
60 key challenges is to simulate the various damages introduced by neutron
61 irradiation. Neutron irradiation could induce a displacement cascade of
62 lattice atoms, and various defects would form with diffusion and
63 combination of the displaced lattice atoms. However, currently neutron
64 irradiation experiments are hampered by long time, expensive cost and high
65 radioactivity [9]. High energy electron irradiation could also induce
66 displacement of lattice atoms that it can be used to simulate the irradiation
67 damage. Although it has a higher irradiation flux and damage rates, it
68 cannot cause the displacement cascade. Also, its penetration depth is thin,

69 and it is usually performed on the foil sample. To some extent, energetic
70 ion irradiation is a promising simulation method, which not only could
71 induce the displacement cascade of lattice atoms, but also has the
72 advantages of high damage rates, minimal residual radio activity and low
73 cost [9]. The application of modern materials modeling methods has also
74 made great progress to study radiation effects on SiC. Y. Katoh et al. [10]
75 has reported the recent advances and outstanding challenges in modeling of
76 radiation induced defects and their interactions with microstructure,
77 transport of fission products through SiC, and thermomechanical properties
78 of SiC, which shows that such modeling can be powerful for the design of
79 SiC-based materials for the harsh environments encountered in fission and
80 fusion applications. Using first-principles density functional theory
81 calculations, N. Daghbouj et al. [11] advanced the understanding of the
82 mechanism of the bubble-to-platelet transition in the He^+-irradiated 6H-SiC.
83 Due to the small size of defect clusters (such as < 1 nm) that they are
84 difficult to measure in traditional TEM, hence, how to measure and
85 quantify their distribution is an outstanding challenge. Recently, C. Liu, I.
86 Szlufarska and their coworker [7] developed a cluster dynamics model that
87 can describe the evolution of irradiation-induced defects, and this mode
88 closes the gap between simulation and experimental results in terms of the
89 cluster size distribution.

90 In the previously reported studies, sufficient effort has been dedicated to
91 investigating the irradiation-induced swelling in SiC. S. Leclerc et al. has
92 reported swelling of He^+-irradiated 4H-SiC at different fluences, different

93 irradiation temperature [12] and different annealing temperature [13]. They
94 have well characterized swelling, disorder and defects evolution in
95 irradiated SiC, moreover, the contribution of different types of defects or
96 damage to swelling was also classified. The disordering behavior, up to
97 amorphization, of both irradiated 6H-SiC and 3C-SiC polytypes was
98 successfully characterized and modelled by A. Debelle et al. [14], and the
99 simulation results were consistent with the experimental results. In these
100 reported results, most investigations were focused on the
101 irradiation-induced isotropic swelling. However, apart from conventional
102 isotropic swelling, irradiation may induce anisotropic swelling in
103 hexagonal-crystal α-SiC [15], which has also been observed in many other
104 hexagonal-crystal ceramic materials including aluminum nitride [16],
105 silicon nitride [17], titanium aluminum carbide [18], and titanium silicon
106 carbide [19]. Besides, it has also been reported that the thermal expansion
107 coefficients of α_{11} is 3.21×10^{-6}, 5.6×10^{-6} and 12.9×10^{-6} (1/℃) for 4H-SiC
108 [20], AlN [21], and Cr2GeC [22], but α_{33} is 3.09×10^{-6}, 6.9×10^{-6}, 17.6×10^{-6}
109 (1/ ℃), respectively. Up to now, the irradiation-induced anisotropic
110 swelling in α-SiC was still insufficient. Compared with isotropic swelling,
111 anisotropic swelling is more deleterious in terms of the resulting
112 degradation of mechanical properties. The swelling itself is not considered
113 a key limitation for the application of SiC in nuclear reactors; however, the
114 significant internal stress induced by differential swelling can lead to
115 degradation of the component structures [18,23,24]. Moreover, fractures or
116 microcracks have also been reported to preferentially occur at the grain

117 boundaries in materials with such anisotropic swelling [18,19]. It appears
118 reasonable that α-SiC and other ceramics with a hexagonal crystal structure
119 may display differing irradiation-induced expansion in different directions,
120 leading to loss of the original crystal integrity and degradation of the
121 mechanical properties. However, α-SiC can also exhibit isotropic swelling.
122 For example, L.L. Snead et al. reported an essentially equivalent dilation of
123 the <a> and <c> axes for neutron-irradiated α-6H-SiC near 60 °C [25]. In
124 addition, Y. Lin and coworkers also observed anisotropic crystal swelling in
125 Si^{2+}-irradiated cubic-β-3C SiC at 1000 °C [26]. Furthermore, the variation
126 of swelling behavior for both α- and β-SiC resulting from different
127 irradiation conditions (different irradiation particles, doses, and
128 temperatures) [25,27,28] complicates the understanding of anisotropic
129 swelling in SiC. To date, the underlying mechanism of this anisotropic
130 swelling remains far from well understood in terms of the physical
131 mechanism and microstructural process.

132 According to the correlation of defects with swelling, with volumetric
133 swelling dominated by various defects, especially point defects or tiny
134 defect clusters at room temperature [7,29], it is reasonable to consider that
135 anisotropic swelling should be correlated to the defect distribution for
136 different crystal orientations. Various attempts have been made to explore
137 the defect distribution and disorder accumulation in irradiated α-SiC. Jiang
138 et al. observed anisotropic lattice expansion in H^+-implanted α-6H-SiC at
139 extremely low doses below 340 K. In that study, the anisotropic swelling
140 was mainly attributed to irradiation-induced vacancies in the basal plane

141 based on a theoretical analysis [27]. However, the defect distribution in the
142 samples was not provided. Zhang et al. [30] observed an anisotropy of
143 disorder accumulation in Au^+-irradiated α-4H-SiC at 165 K using
144 Rutherford backscattering spectroscopy, which was well explained by the
145 stable defect configuration with most interstitial configurations parallel to
146 the [0001] direction according to the molecular dynamic simulation.
147 However, it is not clear that this anisotropic disorder accumulation occurs
148 for anisotropic or isotropic swelling in SiC. Therefore, to obtain insight into
149 the anisotropic swelling mechanism, a fundamental understanding of the
150 detailed defect distribution for different orientations or planes in SiC with
151 anisotropic swelling is needed. However, the defect distribution in α-SiC
152 with anisotropic swelling has rarely been reported because of the relatively
153 small size of the defects, which are difficult to observe using conventional
154 transmission electron microscopy (TEM), especially at relatively low
155 irradiation temperature [7].

156 Kondo et al. [31] explored the stable surface class in 6H-SiC by
157 analyzing nano-void shapes using TEM, which suggests that the
158 observation of some second-type defects formed by the accumulation of
159 point defects might provide insight into the defect distribution in irradiated
160 α-SiC. In addition, in our previous study, anisotropic swelling or strain was
161 introduced in 4H-SiC using selected-area ion irradiation, as demonstrated
162 by atomic force microscopy and electron back scattering diffraction
163 (EBSD) [32]. Hence, this approach might be useful to explore the
164 phenomenon and underlying mechanism of anisotropic swelling in SiC. In

the current study, anisotropic swelling was introduced in 4H-SiC using selected-area ion irradiation, and the defect distribution in different directions was explored using various TEM techniques. An anisotropic defect distribution was observed in the irradiated 4H-SiC. In addition, the potential mechanism for this defect distribution is discussed.

2. Experimental procedures

Single-crystalline n-type 4H-SiC (0001) substrates (Xiamen Powerway Advanced Material Co., Ltd., Xiamen, China) with dimensions of 10 × 10 × 0.33 mm^3 were irradiated with 100-keV He^+ at room temperature to fluences of 1×10^{15} and 5×10^{16} cm^{-2}. During irradiation, the irradiation flux was kept at a level of 6.2×10^{12} $He\cdot cm^{-2}\cdot s^{-1}$, and the beam raster scanning was performed to reach a homogeneous irradiation condition in the irradiated area.

For comparison, both selected-area irradiation and non-selected-area irradiation were performed. During selected-area irradiation, part of the sample was covered by a mask with a hole 8 mm in diameter to clearly distinguish between the irradiated and unirradiated areas. More details of the selected-area ion irradiation procedure are provided in Ref. [32]. The non-selected-area irradiation, i.e., without using the mask, was also prepared at room temperature with a fluence of 5×10^{16} cm^{-2}. The damage and injected helium profile for He^+ into SiC were calculated using SRIM 2013 in full-cascade mode. The sample density and threshold displacement energy for the C and Si sub-lattices used in the calculation were 3.21 $g\cdot cm^{-3}$ and 21 and 35 eV [33], respectively. The total penetration depth

189 predicted by simulation was approximately 600 nm, and the highest
190 damage was predicted to occur at approximately 450 nm with a dose of
191 about 4.2 dpa (displacement per atom, dpa) for the fluence of 5×10^{16} cm^{-2}
192 [34]. In addition, a peak helium concentration of about 2.95% is observed
193 at about 470 nm in depth.

194 After irradiation, cross-sectional thin foils for TEM were prepared from
195 irradiated areas using gallium ions in a focused-ion-beam system (JEOL,
196 JEM-90320FIB). The ion accelerating voltage was 30 kV, and the samples
197 were thinned to a final thickness of about 100 nm. To minimize the damage
198 introduced into the TEM samples by gallium ions during FIB, these TEM
199 samples were then polished by lower energy Ar ions using GentleMill
200 (TECHNOORG-lINDA ltd. Co., Gentle Mill IV8 HI). Both sides of TEM
201 samples were polished with a 1.5 kV beam at 8º incident angle for 40 mins,
202 then 0.5 kV at 15º for 30 mins. The microstructural features of the
203 irradiated 4H-SiC were observed using TEM (JEOL, JEM-2000FX) at an
204 operation voltage of 200 kV. The average size and number density of
205 defects were counted and calculated from weak-beam dark-field TEM
206 images, with 3–5 images used for each calculation. The TEM images used
207 for damage counting are all taken at the same magnification, then adjusted
208 to the same background contrast and brightness using Gatan
209 DigitalMicrograph. The BSDs were then marked by Adobe Photoshop
210 based on the contrast difference from the background, which could be
211 automatically counted using the software of MAC-View Version.4
212 (Mountech Co., Ltd.). The average size of a BSD was recorded by the

213 Heywood diameter. The thicknesses of the observation regions were
214 measured using electron energy loss spectroscopy (EELS) with a
215 Cs-corrected scanning transmission electron microscope (FEI, Titan G2
216 60-300). High-resolution TEM (HR-TEM) analysis, high-angle annular
217 dark field (HAADF) and annular bright field (ABF) scanning transmission
218 electron microscopy (STEM), and core-loss EELS studies were also
219 performed using the Cs-corrected STEM. The operation voltage was 300
220 kV. HAADF- and ABF-STEM images were simultaneously obtained with a
221 17.8-mrad semi-convergence angle and 50–200 and 10.36–24.48 mrad
222 collection angles for the HAADF and ABF mode, respectively.

223 Together with the strain, the elastic stress in the irradiated area was also
224 determined using EBSD and Crosscourt3 software with the elasticity
225 coefficients of 4H-SiC. A field-emission scanning electron microscope
226 (JEOL JSM–7001FA) equipped with an EBSD detector was used to obtain
227 EBSD patterns, operating at an acceleration voltage of 20 kV, a sample tilt
228 of 70°, and a scan size and scan step of 20×20 μm^2 and 0.1 μm, respectively.
229 The elasticity coefficients provided by the Crosscourt3 software, C11=501
230 GPa, C12=111 GPa, C13=52 GPa, C22=501 GPa, C33=553 GPa, and
231 C44=163 GPa, were consistent with previously reported results [35]. The
232 stress was determined by analyzing the EBSD patterns using the
233 CrossCourt3 software. Details of this strain/stress measurement method
234 using EBSD and the strain results have been published elsewhere (Ref.
235 [32]).

236 Electron irradiation of thin-foil 4H-SiC samples using a multi-beam

237 ultra-high voltage electron microscope (multi-beam HVEM, JEOL,
238 JEM-ARM1300) was also performed. The TEM samples for electron
239 irradiation were prepared from unirradiated areas of the selected-area
240 He^{+}-irradiated 4H-SiC samples using FIB; before electron irradiation, the
241 TEM samples were annealed at 600 °C for 30 min in the multi-beam
242 HVEM to remove any potential internal stress. The electron irradiation was
243 performed at room temperature at an accelerating voltage of 1.25 MV with
244 an irradiation area diameter of approximately 2 μm. The electron flux was
245 approximately 1.2×10^{24} $e\cdot m^{-2}\cdot s^{-1}$, and the total irradiation time was 1 h.
246 During irradiation, the electron beam was controlled to be parallel to the
247 $[11\bar{2}0]$ orientation. After electron irradiation, the defect distribution in
248 electron-irradiated thin-foil 4H-SiC samples was also characterized using
249 200-kV TEM (JEOL, JEM-2000FX).

250 **3. Results**

251 3.1 Microstructure in He^{+}-ion-irradiated 4H-SiC

252 After irradiation, the internal microstructure of the He^{+}-implanted 4H-SiC
253 with a fluence of 5×10^{16} cm^{-2} was examined, as shown in Fig. 1(a) together
254 with the simulated damage and He^{+} distribution profiles obtained using
255 SRIM 2013. Because of the different irradiation damage levels, three types
256 of regions with distinct bright-field image contrast (gray, black, and white)
257 are discernible in Fig. 1(a), denoted as the A, B, and C layer, respectively,
258 with the B layer further separated into B_1 and B_2 layers. As indicated by the
259 TEM image contrast and selected-area diffraction, the near-surface layer (A
260 layer) with gray contrast contained only minimal damage and still

261 maintained good crystallinity (as observed in Fig. 1(b)). However, in the
262 highest damage region, where the contrast was white (C layer), an
263 amorphous state was confirmed by observation of the diffraction, as shown
264 in Fig. 1(c). In addition, the two black layers (B_1 and B_2 layers) adjacent to
265 the amorphous layer appear to contain significant defects.

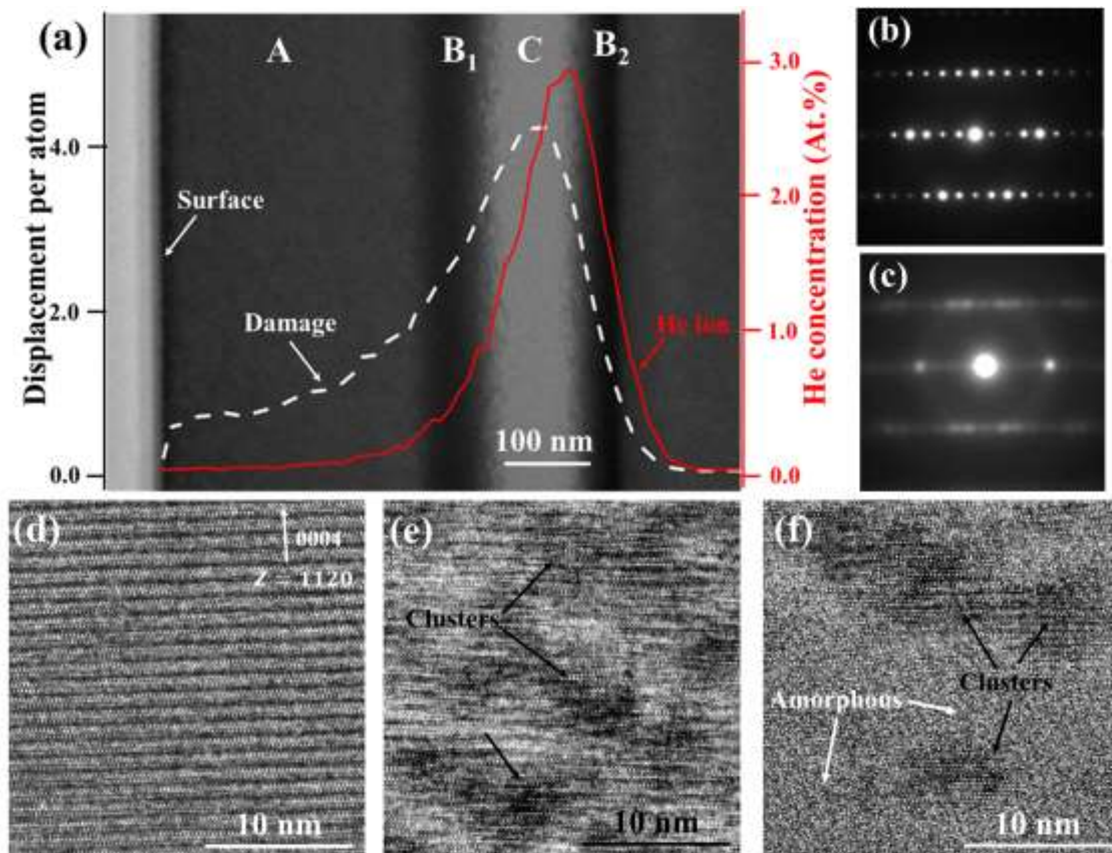

266

267 Fig. 1. Internal microstructure distribution of He^+-irradiated 4H-SiC up to a fluence of 5
268 $\times$ 10^{16} cm^{-2}. (a) Cross-sectional micrograph of He^+-implanted 4H-SiC and depth
269 distribution of displacement damage (white dashed line) and He concentration (red solid
270 line). (b, c) Diffraction patterns corresponding to the (b) A layer and (c) C layer. (d-f)
271 High-resolution TEM images obtained from different regions: (d) A layer, (e) B_1 layer,
272 and (f) near the interface between the B_1 and C layer. The images were taken near the
273 $[11\bar{2}0]$ zone axis.

274

275 To resolve the defects in each region, HR-TEM images were obtained
276 along the $[11\bar{2}0]$ zone axis, which are displayed in Fig. 1(d-f), with Fig.
277 1(d), 1(e), and 1(f) corresponding to the A layer, B_1 layer, and the interface
278 between the B_1 and C layer (amorphous/crystal interface), respectively. In
279 the A layer, the basal plane structure was maintained, which agrees well
280 with the diffraction analysis shown in Fig. 1(b). In addition, the contrast of
281 a few defects can be observed in Fig. 1(d). The main defects in the surface
282 region might be point defects or tiny defect clusters that are difficult to
283 clearly distinguish using HR-TEM [28]. However, in the relatively
284 high-damage region (B_1 layers), the crystal exhibited obvious disorder (Fig.
285 1(e)). Black spots are clearly observed in this image, which are so-called
286 black spot defects (BSDs) [7,11,36], a type of point-defect clusters
287 composed of vacancies and interstitials in irradiated SiC. A small fraction
288 of these black spots may also correspond to small dislocation loops
289 according to previously reported results [37]; however, here, we consider
290 all of them to be BSDs for convenient discussion. Fig. 1(f) shows the
291 microstructure near the amorphous/crystal interface; BSDs are also visible,
292 and some even appear in the amorphous region like an island.

293 3.2 Defect distribution

294 The presence of lattice defects in crystalline materials leads the planes
295 close to the defects to bend. Bending of the lattice planes results in a
296 change of diffraction and therefore a change in the image contrast;
297 information about the defects can thus be obtained by studying the contrast

298 in TEM [38]. To identify characteristics of the defect clusters (BSDs),
299 different reflections corresponding to different sets of lattice planes were
300 used to explore the defect distribution in selected-area He^{+}-irradiated
301 4H-SiC. The distributions of BSDs under different TEM two-beam
302 observation conditions are presented in Fig. 2, with Fig. 2(a, b) obtained at
303 diffraction vector g = [0004] and Fig. 2(c, d) obtained at g = $[11\bar{2}0]$. These
304 images were obtained from the same area, and for orientation, a mark was
305 made by focused-electron-beam irradiation using a JEM-2000FX (200 kV).
306 Under the two-beam observation condition, the BSDs were clearly
307 observed in both the bright-field and dark-field images as black spots (Fig.
308 2(a) and 2(c)) and white spots (Fig. 2(b) and 2(d)), respectively. Comparing
309 the images in Fig. 2(a) and (b) with those in Fig. 2(c) and (d), it is apparent
310 that more BSDs appeared in the [0004] direction (Fig. 2(a) and (b)) than in
311 the $[11\bar{2}0]$ direction (Fig. 2(c) and (d)). Moreover, the defects observed
312 with the reflection vector of [0004] became invisible with the reflection
313 vector of $[11\bar{2}0]$, marked by a white square, and vice versa (marked by a
314 red circle). The details of the lattice-plane bending generally depend on the
315 characteristic of the defect [38]. According to the $\boldsymbol{g} \cdot \boldsymbol{b} = 0$ invisible
316 criterion for planar defects [39-41], the defects observed in Fig. 2 should be
317 a type of planar defect that formed in the corresponding orientation or
318 plane. Similar results were also observed for the reflection vectors g =
319 [0004] and g = $[10\bar{1}0]$ (Fig. S1 in supplementary material), with BSDs
320 observed in one direction becoming invisible in the other direction. Hence,
321 in these samples, the observed BSDs under different diffraction conditions

322 appeared to be the plane defects formed in each reflecting plane.

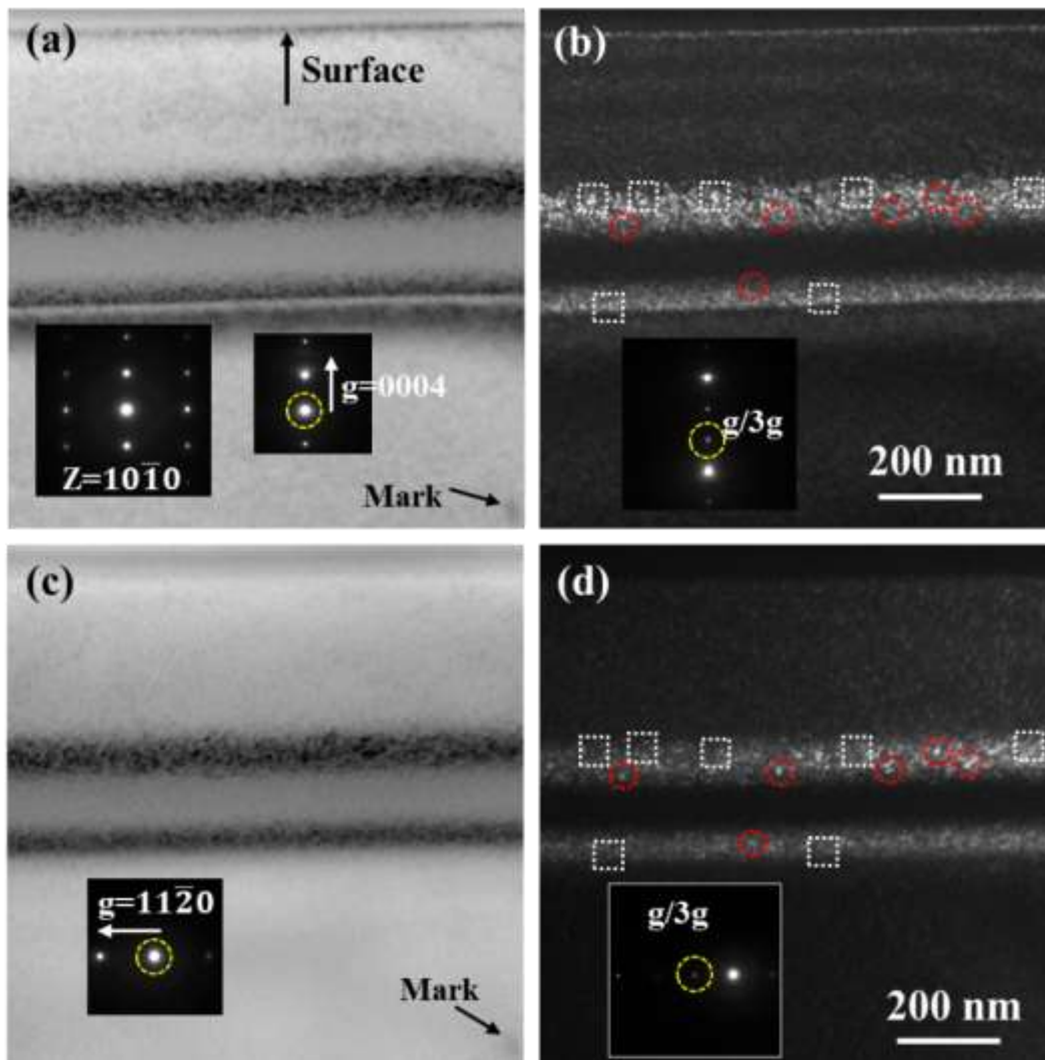

323

324 Fig. 2 TEM images of BSDs under different two-beam observation conditions: (a, b)
325 g=0004 and (c, d) g=11$\bar{2}$0, with (a, c) bright-field images and (b, d) weak-beam
326 dark-field images, g/3g. These images were obtained from the same area with a mark
327 made for orientation purposes.

328

329 More detailed comparison of the defects formed in different orientations
330 or planes was performed, as shown in Fig. 3. The images in Fig. 3(a)–(c)
331 were obtained from the same area with Fig. 3(a) in the two-beam bright

332 field condition (diffraction condition g=0004) and Fig. 3(b) and 3(c) in
333 different weak-beam dark-field conditions (g/3g, with g=0004 for (b) and
334 g=$10\bar{1}0$ for (c)). The images in Fig. 3(d) and 4(e) were also obtained from
335 the same area in different weak-beam dark-field conditions with g/3g and
336 g=0004 for Fig. 3(d) and g=$11\bar{2}0$ for Fig. 3(e).

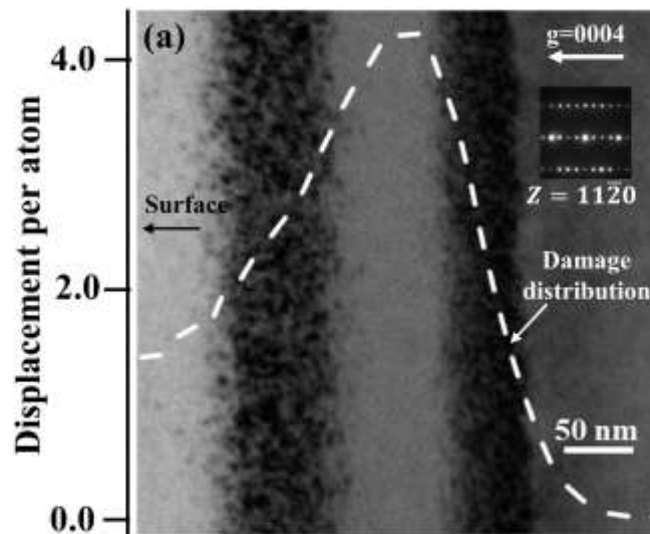

337

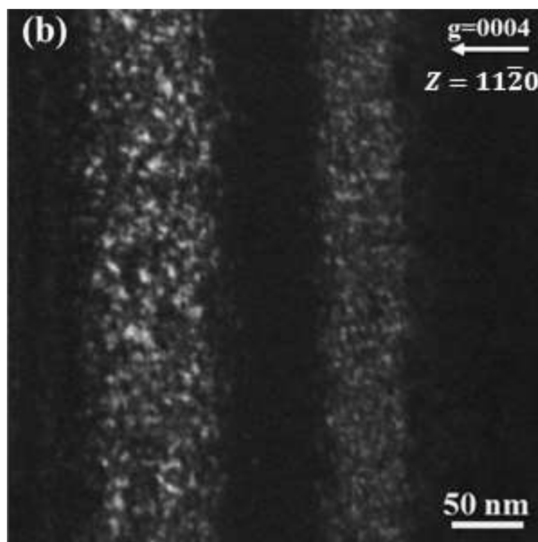

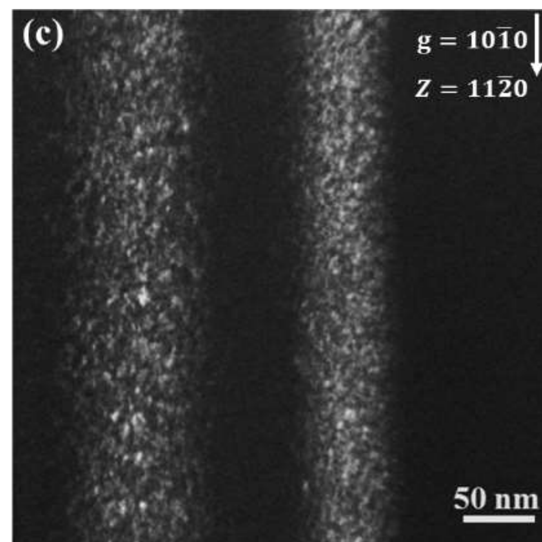

338

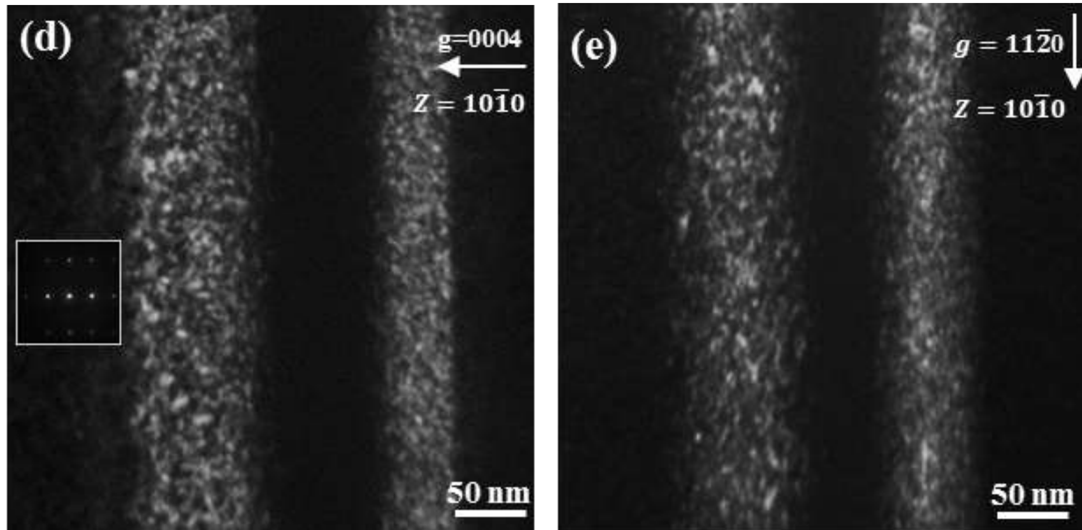

Fig. 3. TEM images of irradiated 4H-SiC taken under different observation conditions. (a–c) were obtained from the same position: (a) two-beam bright-field image and (b, c) g/3g weak-beam dark-field images with g=0004 for (b) and g=$10\bar{1}0$ for (c). (d, e) were obtained from same position with g/3g weak-beam dark field and g=0004 for (d) and g=$11\bar{2}0$ for (e).

These images show the different distributions of BSDs under different diffraction conditions (g=0004, g=$10\bar{1}0$, and g=$11\bar{2}0$) in terms of the defect size and number density. The average size and number density of BSDs in region B_1 with different diffraction conditions were counted using weak-beam dark-field images, and the results are summarized in Table 1. The BSDs appearing in the [0004] direction had the highest number density followed by those in the [$11\bar{2}0$] and [$10\bar{1}0$] directions, and the average size of BSDs formed in the [0004] direction was also substantially larger than that in the [$11\bar{2}0$] and [$10\bar{1}0$] directions. In Fig. 4(a), the BSD size distribution profiles for the [$10\bar{1}0$], [$11\bar{2}0$], and [0004] directions greatly

differ. Although the peak of the profile of the $[10\bar{1}0]$, $[11\bar{2}0]$, and [0004] directions occurred at approximately 4 nm, the number density of relatively large-size BSDs (≥8 nm) was highest in the [0004] direction. In particular for the $[10\bar{1}0]$ profile, there was a lack of relatively large BSDs (≥8 nm). These results suggest an anisotropic defect distribution in the selected-area ion-irradiated 4H-SiC, and the anisotropy of the BSD distribution can be summarized as more and larger BSDs preferentially forming in the [0004] orientation compared with in the $[10\bar{1}0]$ and $[11\bar{2}0]$ orientations.

Table 1 Average size and number density of BSDs in different orientations. The error bars represent the standard deviations

Conditions		$11\bar{2}0$	$10\bar{1}0$	0004
Selected-area ion irradiation	Average size (nm)	4.5 ±0.78	3.9 ±0.52	5.5 ±0.33
	Number density (10^{22} m^{-3})	1.6 ±0.15	1.1 ±0.18	2.9 ±0.28
Non-selected-area ion irradiation	Average size (nm)	4.7 ±0.35	5.0 ±0.58	4.7 ±0.52
	Number density (10^{22} m^{-3})	3.1 ±0.62	2.7 ±0.45	3.5 ±0.68
Electron irradiation	Average size (nm)		6.2 ±0.39	7.1 ±0.17
	Number density (10^{22} m^{-3})		0.72 ±0.018	1.1 ±0.015

369

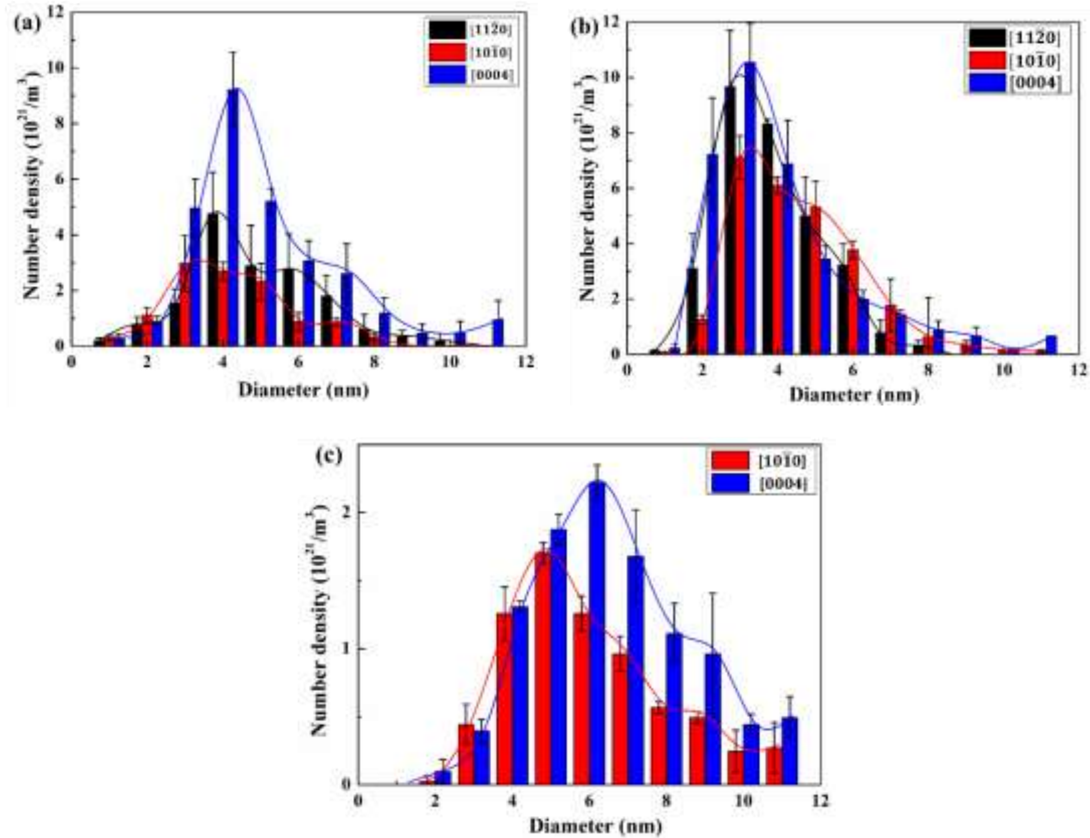

370

371 Fig. 4. Size distribution of BSDs in different orientations: (a) selected-area
372 ion-irradiated sample, (b) non-selected-area ion-irradiated sample, and (c)
373 electron-irradiated thin-film TEM sample. The error bars represent the standard
374 deviations.

375

376 ## 3.3 Nature of defect type

377 The nature of the irradiation-induced defect clusters was explored using
378 ABF-STEM and HAADF-STEM. HAADF-STEM is a robust technique for
379 identifying the position of atoms and atomic columns. When applied in a
380 restricted zone-axis orientation, the contrast in a HAADF image is strongly
381 dependent on the atomic number (Z^n, where $n \approx 1.7$) and the local thickness
382 [42], which provides an approximate method for identifying atomic species.

383 ABF-STEM imaging can also be used to directly detect the position of
384 atoms [43], providing a complementary contrast to HAADF, as shown in
385 Fig. 5. For instance, the Si atom columns correspond to the black spots in
386 the ABF-STEM images and the bright spots in the HAADF-STEM images.

387 The ABF- and HAADF-STEM images in Fig. 5(b) and (c) were
388 obtained from the same region in the A layer (Fig. 1(a)), which was
389 relatively less damaged. Compared with the STEM-ABF image obtained
390 from the unirradiated area (Fig. 5(a)), the defect-induced contrast variation
391 in the STEM image can be clearly observed even in this low-damage
392 region, with some areas becoming relatively blacker and brighter in the
393 ABF (Fig. 5(b)) and HAADF image (Fig. 5(c)), respectively. This can be
394 attributed to the lattice disorder induced by the tiny defect clusters [44].
395 The areas of tiny defect clusters are circumscribed by a dashed line, and the
396 locations of these areas in the ABF and HAADF images agree well.
397 To clearly display the contrast variation, parts of the areas from Fig. 5(b)
398 and (c) were enlarged and are presented in Fig. 5(e) and (f), respectively;
399 the image in Fig. 5(d) (enlarging from Fig. 5(a)) is provided as a
400 comparison standard. Using Gatan Digital Micrograph software, the
401 measured average (0004) plane spacing from an inverse fast Fourier
402 transform (IFFT) pattern in the unirradiated area is approximately 2.47 Å,
403 as shown in Fig. 5(d), almost the same as the previously reported result of
404 2.51 Å determined using XRD [45]. However, in the area with contrast
405 change, the lattice plane spacing was increased to approximately 2.72 Å on
406 average. The expansion of the lattice plane might be attributed to the tiny

interstitial-type cluster formed in these areas [46]. In addition, the area with contrast variation in the HAADF image marked by a solid line in (Fig. 5(c)) was enlarged and is displayed in Fig. 5(f). The difference in image contrast is corroborated by the intensity profiles displayed beneath the corresponding columns, which were obtained using Gatan DigitalMicrograph software across the column along the arrow direction. The intensity of the center columns of this selected area increased. As there was no heavier atom doped into the materials, the increased contrast might arise from the interstitial-type clusters [(47),48)]. The ABF- and HAADF-STEM results for the A layer suggest that most of the tiny defect clusters observed in the A layer should be interstitial-type defects.

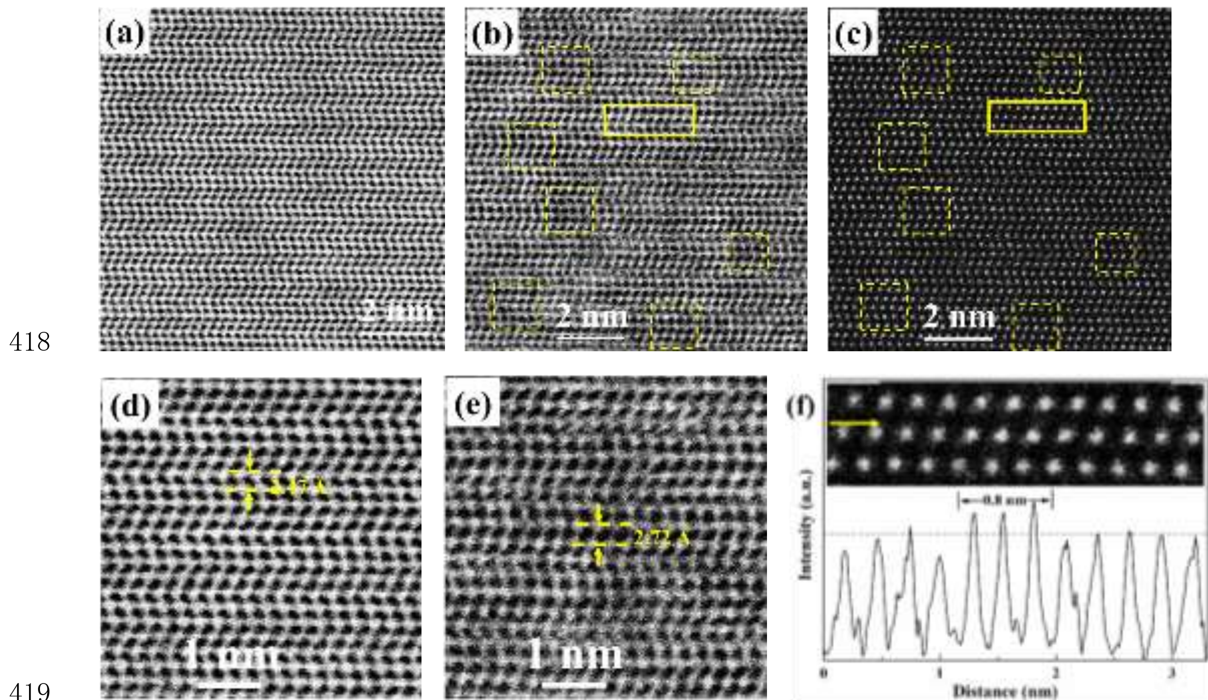

Fig. 5. STEM images obtained from unirradiated area and A layer along the $[11\bar{2}0]$ zone axis. (a) ABF image from unirradiated area. (b) ABF image and (c) HAADF image obtained from same region in the A layer. (d) Enlarged image of the area in (a). (e)

Enlarged image of the area in (b). (f) Enlarged image of the area marked by the solid line in (c) and the intensity of each atom column along the arrow direction. The contrast-changed areas are marked by dashed lines and solid lines.

BSDs are usually identified in HR-TEM images by the black image contrast, as observed in Fig. 1(e). Comparing the ABF-STEM image and HR-TEM image in the same area (Fig. S2 in supplementary material), it is apparent that the BSDs also appeared as black contrast in the ABF-STEM image.

Using ABF- and HAADF-STEM, some larger contrast-changed areas circumscribed by dashed lines were observed in the B_1 layer and near the amorphous/crystal interface, as shown in Fig. 6. These contrast-changed areas can be attributed to the BSDs. In addition, the average size of these contrast-changed areas in Fig. 6 is approximately 5 nm, agreeing well with the size of BSDs summarized in Table 1, which also supports their designation as BSDs. The lattice-plane spacing was also expanded in these areas. Moreover, in some areas, such as in Fig. 6(c), which was enlarged from the area in Fig. 6(b) circumscribed by the red solid line, some extra planes of atom columns were observed, as confirmed by the IFFT image of this area (Fig. 6(d)). These extra planes also indicate that most defects formed in the contrast-changed areas should be interstitial type. Therefore, the above results suggest that the BSDs formed in our samples should mainly be interstitial-type clusters, which is consistent with the mobility of interstitials and vacancies in SiC. Bockstedte et al. reported that the

447 migration energies of vacancies are 3.2–3.6 eV and 3.5–5.2 eV in Si and C
448 [49], respectively, whereas the migration energies of interstitials have been
449 reported to be 1.53 eV in Si and 0.74 eV in C [50]. The Si vacancies in SiC
450 become sufficiently mobile at 800 °C–900 °C [51], and C vacancies may
451 require a higher temperature. It should be pointed out that interstitials are
452 believed to be immobile based on the thermal equilibrium dynamics at
453 room temperature. However, it has also been reported that during the
454 ballistic collision process, the energy deposition from ions to a crystalline
455 could also cause local heating (i.e., an elastic thermal spike) and intense
456 ionization that can lead to localized electronic excitations and local lattice
457 heating (i.e., an inelastic thermal spike). Besides, experimental results have
458 demonstrated that this energy deposition could result in defect formation,
459 diffusion and local structures driven far from equilibrium [52]. Recently, it
460 has also found that the associated defects recovery and diffusion, due to the
461 inelastic thermal spike and localized electronic excitation, are independent
462 of ambient sample temperature [53]. Moreover, molecular dynamics
463 simulation has confirmed the enhanced fission gas diffusion in UO_2 due to
464 the ionization-induced thermal spike [54]. Therefore, the defect clusters
465 (i.e., BSDs) formed in our samples might be attributed to the
466 irradiation-enhanced defect diffusion. As interstitials have a lower
467 migration energy barrier compared with vacancies, they could relatively
468 easily move and combine into clusters in our study. In addition, M.
469 Bockstedte et al. [55] investigated the annealing of vacancies and
470 interstitials in SiC by an ab initio method based on density-functional

theory, which found that the higher mobility of carbon and silicon interstitials compared to the vacancies at lower temperatures drives the formation of interstitial carbon clusters. C. Liu et al. [7] developed a cluster dynamic model by regarding the BSD as an interstitial cluster and proposing additional physical phenomena likely to be present in irradiated SiC. The cluster distributions predicted by their simulations yield an agreement with those measured experimentally, which also supports that BSDs are interstitial type defects.

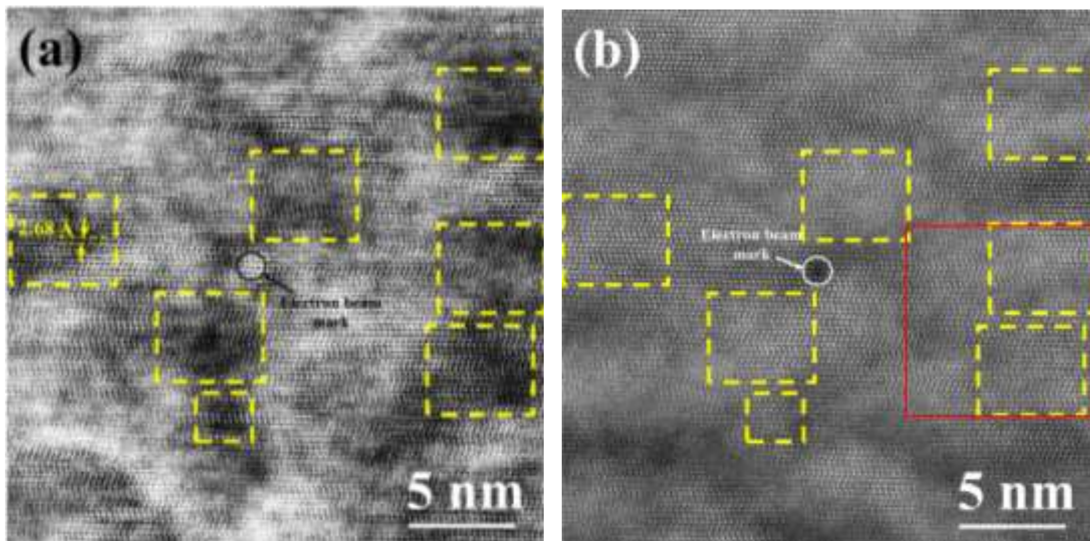

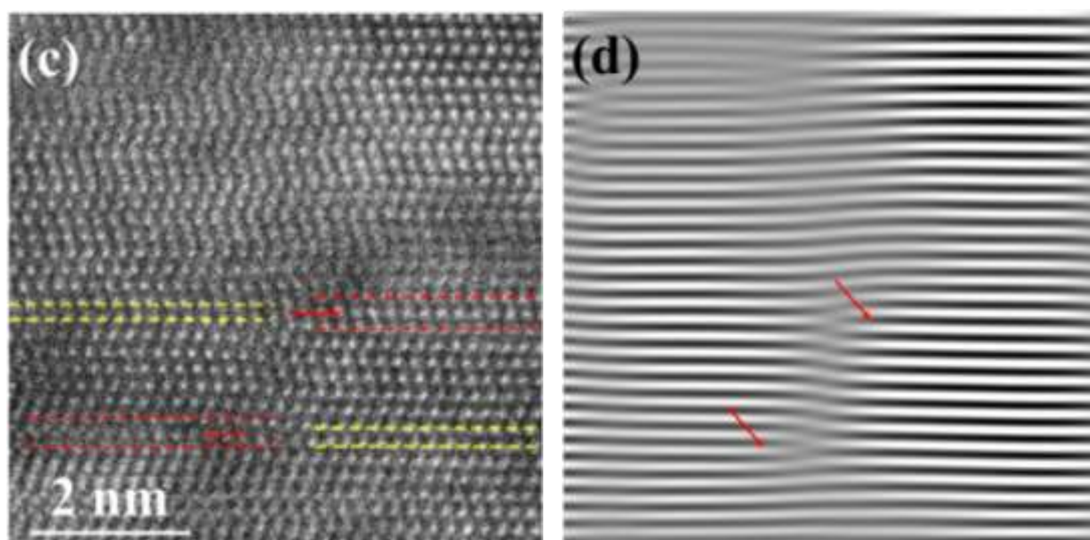

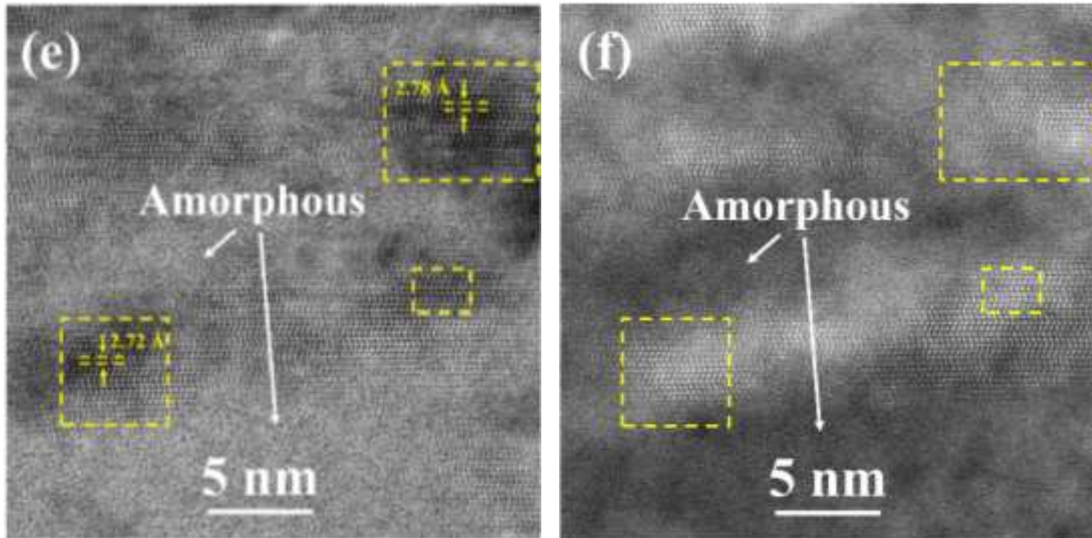

Fig. 6. STEM image obtained from B_1 layer and near the amorphous/crystal interface along the $[11\bar{2}0]$ zone axis. (a, b) were obtained from same region in the B_1 layer: (a) ABF image and (b) HAADF image. (c) is enlarged from the area in (b) circumscribed by the red solid line. (d) Image of inverse fast Fourier transform of (c). (e, f) were obtained from the same region near the amorphous/crystal interface: (e) ABF image and (f) HAADF image. In (a) and (b), a mark was made by an electron beam to confirm the position of each image.

4. Discussion

4.1 Anisotropic defect distribution

The samples in the current study were selected-area ion irradiated such that SiC could freely expand in the Z direction with swelling in the lateral direction (X and Y directions) constrained. These conditions resulted in anisotropic strain or swelling in the sample with a tensile strain in the Z direction and compressive strain in the X and Y directions. The X, Y, and Z directions correspond to lattice orientations of $[11\bar{2}0]$, $[10\bar{1}0]$, and [0004] in these samples, respectively [32].

The anisotropic BSD distribution was determined using conventional TEM, and these defect clusters should mainly be interstitial type in view of the STEM results and defect mobility in SiC. As BSDs correspond to the accumulation of point defects, the formation of more and larger BSDs in the [0004] orientation implies that more interstitial defects were preferentially redistributed in the [0004] orientation compared with in the other two orientations. The defect distribution is correlated to the strain/swelling in the sample. In general, interstitial defects cause the expansion of the lattice around them. The detected defect distribution implies that the tensile strain introduced in the [0004] orientation should be higher than that in the other two orientations. This deduction agrees well with the anisotropic strain condition of our samples with tensile strain in the [0004] orientation and compressive strain in the $[10\bar{1}0]$ and $[11\bar{2}0]$ orientation [32]. Moreover, even though with relative lower number density, the BSDs in the $[10\bar{1}0]$ and $[11\bar{2}0]$ direction are still expected to expand the lattice of the corresponding direction, compressive strain is introduced in these two directions. This implies that more defects with negative volume effect, i.e., vacancy [56] and/or carbon antisite defects (carbon atom occupying the Si-vacancy site, C_{Si}) [4,27,57], than interstitial defects should be introduced in these two directions. It is well known that vacancies are simultaneously introduced into SiC with interstitials; however, the presence of C_{Si} defects remains unclear.

Fig. 7(a) and (b) display the STEM-EELS core-loss spectra of the silicon $L_{2,3}$-edge and carbon K-edge, respectively, acquired from different

522 damaged layers. To facilitate identification, the reference spectra of
523 single-crystal silicon and amorphous carbon are also presented in Fig. 7(a)
524 and 7(b), respectively. The core-loss of EELS spectrum could provide the
525 insight into the bonding structure of materials with its peak position and
526 peak shape. For the SiC crystal lattice structure, it is tetrahedral that the
527 carbon atom is surrounded by four silicon atoms, corresponding to the sp^3
528 mode with the bond of C–Si, and this bonding structure shows the 1s→σ*
529 peak at about 290 eV of the core-loss carbon K-edge spectrum, such as the
530 spectrum of “Unirr” in the Fig. 7(b). For amorphous carbon, it shows the
531 graphite like structure that carbon atom is surrounded by three carbon
532 atoms, corresponding to a sp^2 configuration, which shows both π* (C=C)
533 and σ* (C–C) peaks at about 283 eV and 295 eV [58,59], respectively, such
534 as the spectrum of “Am. C” in the Fig. 7(b). It is clear that the transition of
535 C-Si bond to C–C and/or C=C bond in the SiC require a displacement of Si
536 atom with C atom, which would result in the formation of C_{Si} (carbon atom
537 occupying the Si-vacancy site), i.e., the appearance of peak at about 283 eV
538 (1s→π*) and 295 eV (1s→σ*) in the carbon K-edge core-loss EELS
539 spectrum would be evidence of the presence of C_{Si}.

540 For the core-loss EELS spectra in the He^+ irradiated SiC, the peaks
541 gradually broadened with increasing damage (from the A to C layer) in
542 terms of the Si $L_{2,3}$-edge peak at ~103 eV (Fig. 7(a)) and the carbon K-edge
543 1s→σ* peak at about 290 eV, especially for the B1 and C layer, which
544 indicates the damage or decreasing of the C-Si tetrahedral bond structure in
545 SiC. As comparing the “unirr” spectrum with the “A” spectrum in the Fig.

(b), it is shown that the left side (280~290 eV) of the σ* peak (290 eV) seems not broadening. However, its right side (290~300 eV) becomes broadened and smoothing, and this energy region just corresponds to the carbon σ* peak (295 eV) of the "Am. C" spectrum. This may suggest the appearance of carbon σ* peak at 295 eV, and also the formation of C–C bond structure and the C_{Si}. With increasing damage, such as the B1 and C layer, the broadening of this peak (290 eV) at the region of 290~300 eV becomes more dominant. Moreover, a 1s→π* shoulder peak (283 eV) was also observed in the spectra acquired from the B1 and C layer, which further confirms the presence of C_{Si} in the selected-area irradiated 4H-SiC. It should be pointed out that the formation of 1s→π* peak (283 eV) indicates the irradiation-induced bonding configuration shifting from sp^3 to sp^2 in SiC, which requires a highly damaged state, such as the formation of defect clusters or amorphization. Thus, it is observed only in the B1 and C layer. The transition of C–Si to C–C (and/or C=C) bond detected in our previous Raman analysis also implies the occurrence of the C_{Si} [32]. In previous works of Kondo et al. [4], an increase in the population of antisite C_{Si} was also observed in Si^{2+}-irradiated SiC fiber, which was implicated as the primary cause for the shrinkage of the irradiated SiC fibers. Considering the negative volume effect of C_{Si} [4,60], the antisite defect of C_{Si} may be dominantly located in ($[11\bar{2}0]$) and ($[10\bar{1}0]$), contributing to the lateral (X- and Y-direction) compressive strain in selected-area ion-irradiated 4H-SiC. Therefore, in the selected-area ion-irradiated 4H-SiC, it is likely that interstitial defects are preferentially redistributed in

570 the freely expanding direction (Z, [0004] orientation) with vacancy and/or
571 carbon antisite defects dominantly located in the constrained swelling
572 direction (X and Y, $[11\bar{2}0]$ and $[10\bar{1}0]$ orientation).

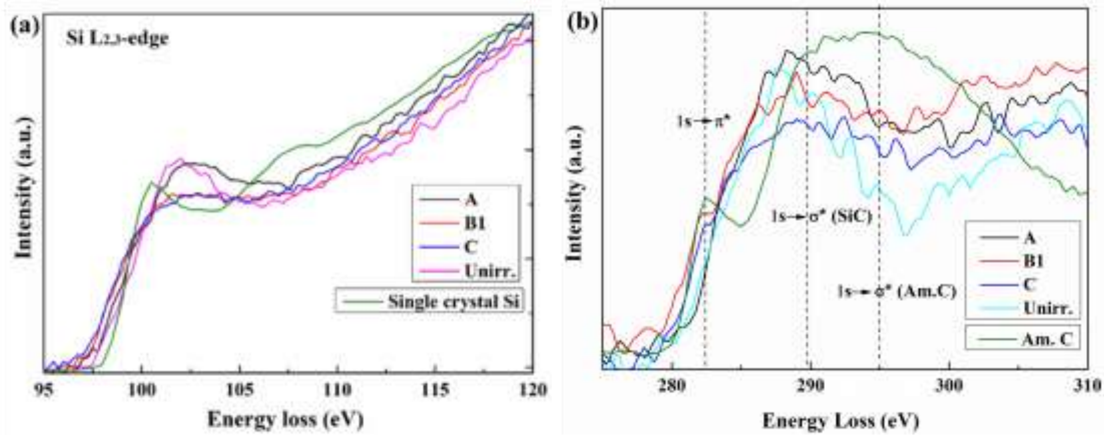

573

574 Fig. 7 Irradiation-induced change of EELS core-loss spectra: (a) Si $L_{2,3}$-edge spectra
575 and (b) carbon K-edge spectra. The inset letters correspond to the layers marked in Fig.
576 1(a). Reference spectra of single-crystal silicon and amorphous carbon obtained from
577 the Gatan EELS website (https://eels.info/atlas/carbon) are provided for ease of
578 identification.

579

580 4.2 Potential mechanism for anisotropic defect distribution

581 The different number density and size distribution of BSDs (shown in
582 Table 1 and Fig. 4(a)) indicate different nucleation and growth conditions
583 for the different orientations or planes. It is apparent that BSDs in the [0004]
584 orientation have more nucleation sites and a higher growth rate. Defect
585 formation and growth in SiC during ion irradiation mainly arise from the
586 irradiation-induced point defects and their diffusion and combination. Ion
587 irradiation usually introduces nearly the same number of interstitials and

588 vacancies (Frenkel pairs) in SiC. The anisotropic defect distribution in our
589 sample can mainly be attributed to the different mobilities of interstitials
590 and vacancies, which usually control the defect type and distribution. As
591 the sample was irradiated at room temperature, where interstitial point
592 defects are mobile and vacancies are not, it is likely that some of the
593 interstitials might be redistributed from the $[10\bar{1}0]$ and $[11\bar{2}0]$
594 orientations to the [0001] orientation to reduce the internal energy because
595 of the habit plane for (0001), resulting in larger and more interstitial-type
596 BSDs in the interplane of [0004].

597 It has been reported that differential swelling leads to significant stresses
598 [18,24]. Using EBSD, the stress distributions in irradiated and unirradiated
599 areas were measured, as shown in Fig. 8 with (b), (c), and (d)
600 corresponding to the stress in the X ($[11\bar{2}0]$), Y ($[10\bar{1}0]$), and Z ([0001])
601 directions, respectively. It is clear that because of the restriction of swelling,
602 great compressive stress was introduced in both the X and Y directions with
603 an average of −0.94 and −1.15 GPa, respectively; however, little stress
604 arose in the Z direction because of the relaxation of swelling. Moreover, the
605 stress distribution in the other sample with substantially lower fluence of
606 1×10^{15} cm^{-2} was also measured by EBSD, as shown in Fig. 9. The
607 anisotropic stress distribution was also distinct in this sample with
608 relatively large compressive stress in the X (−0.23 GPa) and Y (−0.36 GPa)
609 directions but little in the Z direction. This result indicates that the
610 compressive stress in the lateral direction begins to accumulate even at the
611 beginning of irradiation. Kondo et al. [61] reported that compressive stress

likely inhibits the interstitial-type loop nucleation in planes perpendicular to the stress axis, resulting in an anisotropic Frank loop development in ion-irradiated SiC. In Table 1 and Fig. 4(a), the BSDs in the lateral direction have a lower number density and smaller size. It is likely that the lateral compressive stress introduced during irradiation inhibits the nucleation and growth of interstitial defects. This anisotropy of the defect distribution in selected-area He^+-irradiated 4H-SiC can be mainly attributed to the different stress conditions in the different directions.

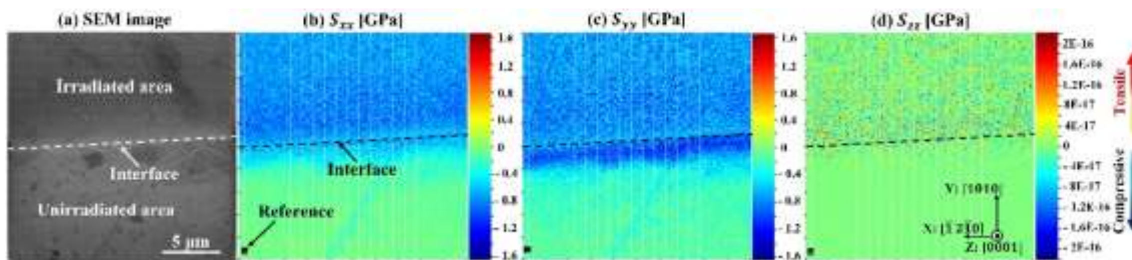

Fig. 8. Stress distribution in selected-area He^+-irradiated 4H-SiC with fluence of 5×10^{16} cm^{-2}: (a) SEM image and (b)–(d) corresponding stress composition in (b) X, (c) Y, and (d) Z direction. The strain distribution in this region is provided in the supplementary materials of Ref. [32].

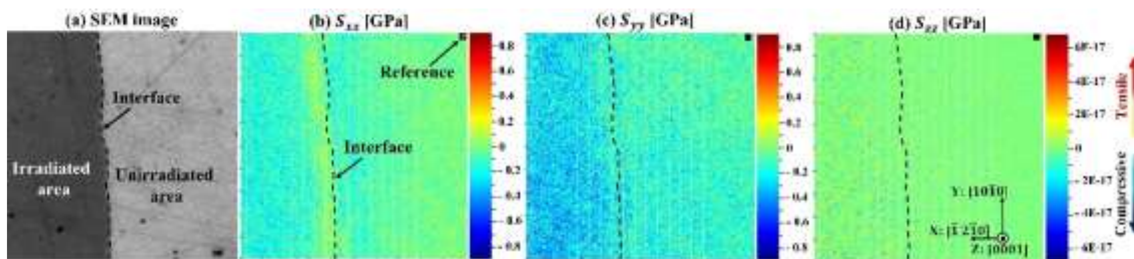

Fig. 9. Stress distribution in selected-area He^+ irradiated 4H-SiC with fluence of 1×10^{15} cm^{-2}: (a) SEM image and (b)–(d) corresponding stress composition in (b) X, (c) Y, and (d) Z direction.

630 4.3 Defect distribution in non-selected-area He^+-irradiated 4H-SiC

631 For comparison, a non-selected-area He^+-irradiated 4H-SiC sample was
632 prepared using the same fluence of 5×10^{16} cm^{-2}. The defect distribution in
633 this sample is shown in Fig. 10. The observed difference in the different
634 directions in this sample appears to be smaller than that in the selected-area
635 irradiated 4H-SiC (Fig. 2). The calculated average size and number density
636 of the BSDs are summarized in Table 1. The BSDs in different directions
637 were similar in average size with a higher number density in the [0004]
638 direction. The defect distribution remained slightly anisotropic in this
639 sample. However, its anisotropy was substantially smaller than that in the
640 selected-area irradiated samples in terms of the average size and number
641 density of BSDs. This result is supported by the similar defect size
642 distributions in the different directions in Fig. 4(b). Without constraint in
643 the lateral direction, the compressive stress introduced in the
644 non-selected-area irradiated sample should be lower than that in the
645 selected-area irradiated sample. The relatively lower anisotropy of the
646 defect distribution in the non-selected-area He^+-irradiated 4H-SiC indicates
647 the restraining effects of the compressive stress on the formation of
648 interstitial defects.

649 Although relatively smaller, an anisotropic defect distribution remained
650 in this non-selected-area irradiated sample. It has been reported that
651 compressive stress would also be introduced in the lateral direction in
652 ion-irradiated SiC, which is attributed to the constraint against lateral
653 expansion owing to the shallow thickness of the irradiated layer compared

654 with the sample thickness in contrast to the free expansion allowed along
655 the surface normal [61]. Hence, the anisotropic defect distribution in the
656 non-selected-area ion-irradiated sample may also be attributed to the
657 compressive stress introduced in the lateral direction.

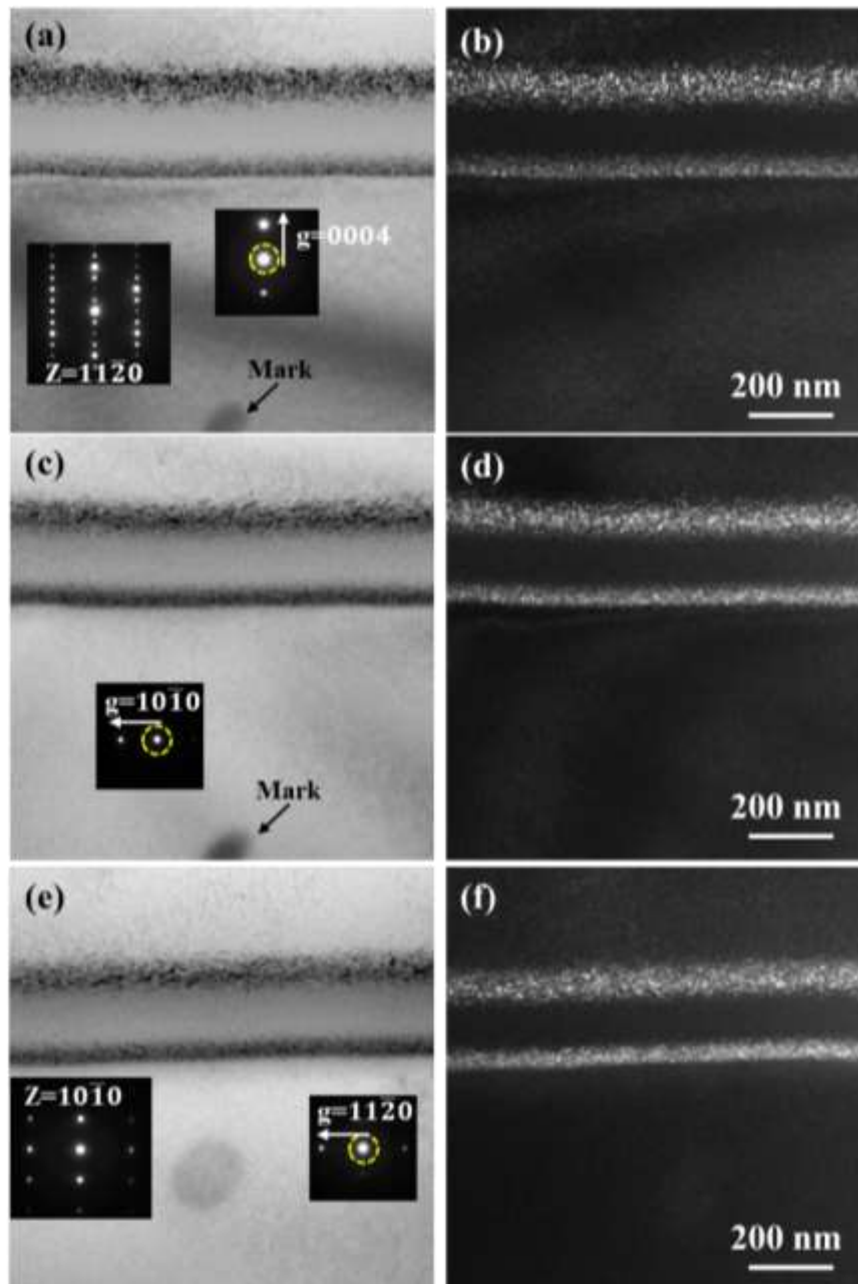

658

659 Fig. 10 TEM images of BSDs in non-selected-area He^{+}-irradiated 4H-SiC with fluence
660 of 5×10^{16} cm^{-2}. (a), (c), and (e) are two-beam bright-field images with g=0004, $10\bar{1}0$,

and $11\bar{2}0$, respectively, and (b), (d) and (f) are their corresponding weak-beam dark-field images with g/3g. (a–d) were obtained from the same area, and (e, f) were obtained from another area.

4.4 Defect distribution in electron-irradiated thin-film 4H-SiC

It has been reported that the introduction of compressive stress in the lateral direction may even be possible in non-selected-area ion-irradiated bulk samples because of the constraint against lateral expansion [61]. For comparison, the electron irradiation was performed on a TEM-foil sample of 4H-SiC at room temperature. Before irradiation, the samples were annealed at 600 °C for 30 min to remove any potential internal stress. During irradiation, the electron beam was parallel to the $[11\bar{2}0]$ zone axis. Hence, compared with the He^{+}-irradiated bulk sample, there were two main differences in terms of the stress condition that should be noted in the electron-irradiated sample. One is that the lateral stress in the electron-irradiated area should be relatively lower because of the relatively thinner electron-irradiated sample, though electron irradiation is also a type of selected-area irradiation. The other is that the [0004] and $[10\bar{1}0]$ orientations should have a similar stress as both are lateral directions as the electron beam was along the $[11\bar{2}0]$ direction. Therefore, the different stress states in the [0004] and $[10\bar{1}0]$ orientations in the ion-irradiated sample could be neglected in this electron-irradiated sample.

The defect distributions in the centers of the electron-irradiated areas are shown in Fig. 11, and the counted average size and number density of

685 BSDs are summarized in Table 1. The size distribution of BSDs is shown in
686 Fig. 4(c). The BSDs formed under electron irradiation were larger in
687 average size and lower in number density than those under ion irradiation.
688 This may be attributed to a larger flux density of electron beam irradiation
689 (1.2×10^{24} $e\cdot m^{-2}\cdot s^{-1}$) compared with the ion irradiation (6.2×10^{16} $He\cdot m^{-2}\cdot s^{-1}$)
690 and also the surface effects of the TEM-foil sample. From the average size,
691 number density, and size distribution of BSDs in the $[10\bar{1}0]$ and [0004]
692 orientations, the defect distribution in electron-irradiated 4H-SiC also
693 appears to be anisotropic. However, the ratios of the average size and
694 number density between the [0004] and $[10\bar{1}0]$ orientation were 1.15
695 (7.1/6.2) and 1.52 (1.1/0.72) (Table 1), respectively, in the
696 electron-irradiated sample, which are substantially smaller than the ratios
697 of 1.41 (5.5/3.9) and 2.64 (2.9/1.1), respectively, in the selected-area
698 He^+-ion-irradiated sample. Therefore, it is apparent that the anisotropy of
699 the defect distribution in the selected-area He^+-irradiated sample was
700 enhanced, which can be primarily attributed to the compressive stress
701 introduced in the lateral direction during irradiation.

702 It should be noted that the different irradiation conditions for ion
703 irradiation and electron irradiation, including the different dose rates,
704 different irradiation particle energies, and the cascade effect, might
705 contribute to the different defect evolution. In particular, interstitial and
706 vacancy atoms might annihilate on the surface of the thin sample used in
707 the electron irradiation, which would greatly affect the defect distribution
708 in the sample. However, the above cases should have a similar effect on the

defect distribution for the [0004] and $[10\bar{1}0]$ directions, and they might not greatly change the anisotropy of the defect distribution between the [0004] and $[10\bar{1}0]$ directions. Hence, the great difference in the anisotropy of the defect distribution between the selected-area ion irradiation and electron irradiation can be mainly attributed to the compressive stress introduced during ion irradiation.

Similar to the non-selected-area He^{+}-irradiated sample, anisotropic defect distribution was also somewhat introduced in the electron-irradiated foil sample. However, the stress effect on the anisotropy should be quite low in the electron-irradiated sample, as discussed above. Stress should not be the primary cause for the anisotropy between the [0004] and $[10\bar{1}0]$ directions in the electron-irradiated sample. Hence, the anisotropic defect distribution in the non-selected-area ion-irradiated sample and electron-irradiated sample might not only be attributed to the stress, and some other potential mechanisms might exist [27,31,62]. Anisotropic swelling is also observed in the reported result that a shrinkage of the a-axis is formed at extremely low doses of 1.26×10^{-3} dpa in H^{+}-irradiated 6H-SiC with an expansion in the c-axis, which could be associated with irradiation-induced vacancies in the a-axis [27]. Therefore, the initial anisotropic distribution of defects in ion-irradiated α-SiC might be attributed to the intrinsic property of α-SiC, such as the larger parameter of the c-axis than that of a-axis. The interstitial atoms would expand the lattice, and the local crystal structure around a vacancy could contract. When a C or Si atom is removed from the lattice site in a unit cell of α-SiC, a local

733 lattice strain is induced, and a repositioning of the surrounding atoms
734 occurs to minimize the internal energy. The anisotropy of defect
735 distribution, i.e., the interstitial atoms redistributed into c-axis (which is
736 larger in plane space) and vacancies and/or C_{Si} located into the a-axis,
737 seemly better to minimize the strain and disorder induced by irradiation.
738 This interpretation agreed with the distribution of interstitial type defect of
739 helium platelet, which has been reported to preferentially form in the c-axis
740 [63]. In addition, the modeling results showed that the activation barrier for
741 a migration of carbon interstitials in the 4H–SiC is the lowest along the
742 c-axis ([0001]) compared with the $[11\bar{2}0]$ and $[10\bar{1}0]$ [64], which also
743 agrees well with the defect distribution in our study. This suggests that the
744 different migration energy for a defect along the different axes in the α–SiC
745 would also contribute to the anisotropic defect distribution and the
746 anisotropic swelling. As the compressive stress is introduced into the a-axis,
747 i.e., selected-area He^{+}-irradiated 4H-SiC, a higher anisotropic defect
748 distribution is observed, which shows an enhanced tendency of defect
749 repositioning discussed above. The compressive stress would compact the
750 plane space in the a-axis, which seemly inhibits the interstitial type defect
751 formation in this direction and enhances the anisotropic defect distribution
752 in the He^{+} irradiated 4H-SiC. In addition, it has been reported that the
753 irradiation-induced tensile strain would cause the drift of interstitial atoms,
754 resulting in a higher tensile strain [65]. Considering the strain condition in
755 the selected-area He^{+}-ion-irradiated 4H-SiC that tensile strain in the [0004]
756 orientation and compressive strain in $[10\bar{1}0]$ and $[11\bar{2}0]$, it is possible

757 that this strain condition would affect defect drift and enhance the
758 anisotropic defect distribution, which would in turn result in higher
759 anisotropic swelling. Therefore, the observed anisotropic defect distribution
760 in the selected-area He^{+}-irradiated 4H-SiC should be attributed to the
761 integrated effects, including both the intrinsic properties of α-SiC and the
762 compressive stress in a-axis.

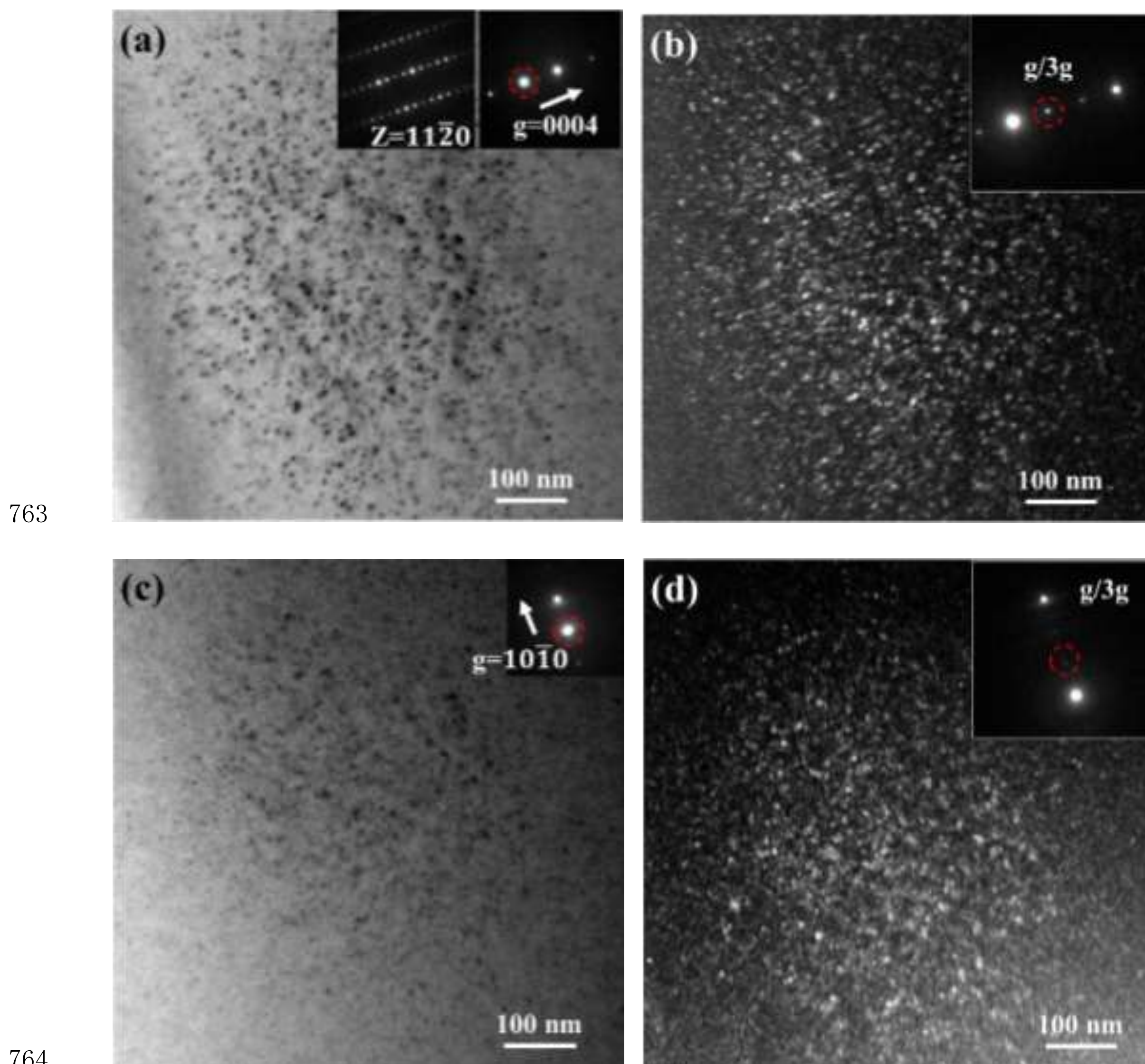

763

764

765 Fig. 11. TEM images of BSD distribution in the center of electron irradiation area of
766 electron-irradiated 4H-SiC: (a, b) g=0004 and (c, d) g=10$\bar{1}$0, with (a, c) bright-field

images and (b, d) weak-beam dark-field images, g/3g. These images were obtained from the same area.

5. Summary

Using TEM techniques, the defect distribution in selected-area He^{+}-irradiated 4H-SiC with irradiation-induced anisotropic swelling was explored, and anisotropy of the defect distribution was observed. Interstitial defects were preferentially redistributed to the freely expanding direction (Z direction, [0004] orientation) with negative volume defects dominantly located in the constrained swelling directions (X and Y directions, $[11\bar{2}0]$ and $[10\bar{1}0]$ orientations). This anisotropy of the defect distribution was substantially larger than that in non-selected-area He^{+}-irradiated 4H-SiC and electron-irradiated thin-foil 4H-SiC. Compressive stress was introduced in the lateral direction (X and Y directions, $[10\bar{1}0]$ and $[11\bar{2}0]$ orientations), with little introduced in the surface normal direction (Z direction, [0004] orientation) in the selected-area He^{+}-irradiated 4H-SiC because of the constraint against lateral expansion, and these compressive stresses were introduced at the beginning of ion irradiation. The compressive stress introduced during irradiation was speculated to inhibit the formation of interstitial defects, enhancing the anisotropic defect distribution in the selected-area ion-irradiated 4H-SiC.

790 **Acknowledgements**

791 This work was partly supported by JSPS KAKENHI Grant Numbers
792 JP19K22035 and JP19H00799. Part of this work was conducted at the
793 Joint-Use Facilities at Hokkaido University, supported by the "Project for
794 promoting public utilization of advanced research infrastructure (Program
795 for supporting introduction of the new sharing system) grant number
796 JPMXS0420100519" and the "Nanotechnology Platform" program of the
797 Ministry of Education, Culture, Sports, Science and Technology (MEXT),
798 Japan. The authors thank Mr. R. Ota for his help with the STEM
799 experiments. Dr. Yang acknowledges stipend support from the Chinese
800 Scholarship Council to perform this work at Hokkaido University. The
801 authors would also like to thank Tiffany Jain, M.S., from Edanz Group
802 (https://en-author-services.edanzgroup.com/ac) for editing a draft of this
803 manuscript.

804

805 **References**

806 [1] Y. Zhang, R. Sachan, O. H. Pakarinen, M. F. Chisholm, P. Liu, H. Xue,
807 W. J. Weber, Ionization-induced annealing of pre-existing defects in silicon
808 carbide, Nat. Commun. 6, 8049 (2015).

809 [2] L. Nuckols, M. L. Crespillo, C. Xu, E. Zarkadoula, Y. Zhang, W. J.
810 Weber, Coupled effects of electronic and nuclear energy deposition on
811 damage accumulation in ion-irradiated SiC, Acta Mater. 199 (2020) 96–
812 106.

813 [3] N. Daghbouj, B. S. Li, M. Callisti, H. S. Sen, J. Lin, X. Ou, M. Karlik,
814 T. Polcar, The structural evolution of light-ion implanted 6H-SiC single
815 crystal: Comparison of the effect of helium and hydrogen, Acta Mater. 188
816 (2020) 609-622.
817 [4] S. Kondo, T. Hinoki, M. Nonaka, K. Ozawa, Irradiation-induced
818 shrinkage of highly crystalline SiC fibers, Acta Materialia 83 (2015) 1–9.
819 [5] N. G. Wright, A. B. Horsfall, K. Vassilevski, Prospects for SiC
820 electronics and sensors, Mater. Today 11 (2008).
821 [6] M. Li, X. Zhou, H. Yang, S. Du, Q. Huang, The critical issues of SiC
822 materials for future nuclear systems, Scr. Mater. 143 (2018) 149–153.
823 [7] C. Liu, L. He, Y. Zhai, P. M. Voyles, K. Sridharan, D. Morgan, I.
824 Szlufarska, Evolution of small defect clusters in ion irradiated 3C-SiC:
825 Combined cluster dynamics modeling and experimental study, Acta Mater.
826 125 (2019) 377–389.
827 [8] Yutai Katoh, Sosuke Kondo, Lance L. Snead, Microstructures of
828 beta-silicon carbide after irradiation creep deformation at elevated
829 temperatures, J. Nucl. Materl. 382 (2008) 170–175.
830 [9] G.S. Was, Z. Jiao, E. Getto, K. Sun, A.M. Monterrosa, S.A. Maloy, O.
831 Anderoglu, B.H. Sencerc, M. Hackett, Emulation of reactor irradiation
832 damage using ion beams, Scrip. Mater. 88 (2014) 33–36.
833 [10] Y. Katoh, L. L. Snead, I. Szlufarska, W. J. Weber, Radiation effects in
834 SiC for nuclear structural applications, Cur. Opin. Sol. State Mater. Sci. 16
835 (2012)143–152.

[11] N. Daghbouj, B.S. Li, M. Callisti, H.S. Sen, M. Karlik, T. Polcar, Microstructural evolution of helium-irradiated 6H–SiC subjected to different irradiation conditions and annealing temperatures: A multiple characterization study, Acta Mater. 181 (2019) 160–172.

[12] S. Leclerc, A. Declémy, M. F. Beaufort, C. Tromas, J. F. Barbot, Swelling of SiC under helium implantation, J. Appl. Phys. 98 (2005) 113506.

[13] S. Leclerc, M.F. Beaufort, A. Declémy, J.F. Barbot, Evolution of defects upon annealing in He-implanted 4 H-SiC, Appl. Phys. Lett. 93 (2008) 122101.

[14] A. Debelle, L. Thome, D. Dompoint, A. Boulle, F. Garrido, J Jagielski, D. Chaussende, Characterization and modelling of the ion-irradiation induced disorder in 6H-SiC and 3C-SiC single crystals, J. Phys. D: Appl. Phys. 43 (2010) 455408.

[15] F.W. Clinard, Jr., W. Dienst, E.H. Farnum, Issues related to mechanical properties of neutron-irradiated ceramics, J. Nucl. Materl. 212-215 (1994) 1075–1080.

[16] I.T. Yano T, Swelling and microstructure of AlN irradiated in a fast reactor, J. Nucl. Materl. 203 (1993) 249–254.

[17] T. Yano, M. Akiyoshi, K. Ichikawa, Y. Tachi, T. Iseki, Physical property change of heavily neutron-irradiated Si3N4 and SiC by thermal annealing, J. Nucl. Materl. 289 (2001) 102.

[18] C.A.C. Silva, C. Shih, T. Koyanagi, Y. Katoh, S. J. Zinkle, Anisotropic swelling and microcracking of neutron irradiated Ti3AlC2–Ti5Al2C3 materials, Scr. Mater. 114 (2016) 74–78.

[19] J.C. Nappé, C. Maurice, Ph. Grosseau, F. Audubert, L. Thomé, B. Guilhot, M. Beauvy, M. Benabdesselam, Microstructural changes induced by low energy heavy ion irradiation in titanium silicon carbide, J. European Ceram. Soc. 31 (2011) 1503–1511.

[20] Z. Li, R. C. Bradt, Thermal expansion of the hexagonal (4H) polytype of SiC, J. Appl. Phys. 60 (1986) 612.

[21] H. Kroncke, S. Figge, B.M. Epelbaum, D. Hommel, Determination of the temperature dependent thermal expansion coefficients of bulk AlN by HRXRD, ACTA Phys. Polon. A, 114 (2008) 1193-1200.

[22] T. H. Scabarozi, S. Amini, O. Leaffer, Thermal expansion of select phases measured by high temperature x-ray diffraction and dilatometry, J. Appl. Phys. 105 (2009) 013543.

[23] S. Kondo, T. Koyanagi, T. Hinoki, Irradiation creep of 3C–SiC and microstructural understanding of the underlying mechanisms, J. Nucl. Materl. 448 (2014) 487–496.

[24] S. Smolentsev, N.B. Morley, M. Abdou, Magnetohydrodynamic and thermal issues of the SiC_f/SiC flow channel insert, Fusion Sci. Technol. 50 (2006) 107–119.

[25] L.L. Snead, Y. Katoh, T. Koyanagi, K. Terrani, E.D. Specht, Dimensional isotropy of 6H and 3C SiC under neutron irradiation, J. Nucl. Materl. 471 (2016) 92–96.

882 [26] Y. Lin, C. Ho, W. Chuang, C. Ku, J. Kai, Swelling of ion-irradiated
883 3C–SiC characterized by synchrotron radiation based XRD and TEM, J.
884 Nucl. Materl. 455 (2014) 292–296.
885 [27] W. Jiang, P. Nachimuthu, W. J. Weber, L. Ginzbursky, Variation in
886 lattice parameters of 6H-SiC irradiated to extremely low doses, Appl. Phys.
887 Lett. 91 (2007) 091918.
888 [28] Y. Zhang, W. J. Weber, W. Jiang, C. M. Wang, V. Shutthanandan, A.
889 Hallen, Effects of implantation temperature on damage accumulation in
890 Al-implanted 4H–SiC, J. Appl. Phys. 95 (2004) 4012.
891 [29] B. Tyburska-Püschel, Y. Zhai, L. He, C. Liu, A. Boulle, P. M.
892 Voyles, I. Szlufarska, K. Sridharan, Size distribution of black spot defects
893 and their contribution to swelling in irradiated SiC, J. Nucl. Materl. 476
894 (2016) 132–139.
895 [30] Y. Zhang, F. Gao, W. Jiang, D.E. McCready, W.J. Weber, Damage
896 accumulation and defect relaxation in 4H-SiC, Phys. Rev. B 70 (2004)
897 125203.
898 [31] S. Kondo, C. M. Parish, T. Koyanagi, Y. Katoh, Equilibrium shapes
899 and surface selection of nanostructures in 6H-SiC, Appl. Phys. Lett. 110
900 (2017) 142106.
901 [32] S. Yang, S. Tokunaga, M. Kondo, Y. Nakagawa, T. Shibayama,
902 Non-destructive evaluation of the strain distribution in selected area He+
903 ion irradiated 4H-SiC, Appl. Surf. Sci. 500 (2020).
904 [33] R. Devanathan, T. Diaz de la Rubia, W.J. Weber, Displacement
905 threshold energies in b-SiC, J. Nucl. Materl. 253 (1998) 47–52.

906 [34] S. Yang, Y. Nakagawa, M. Kondo, T. Shibayama, electron energy-loss
907 spectroscopic evaluation of depth-dependent swelling of He+ ion-irradiated
908 4H-SiC correlated with defect type, J. Appl. Phys. 127 (2020) 175106.
909 [35] K. Kamitani, M. Grimsditch, J.C Nipko, C.K. Loong, M. Okada, I.
910 Kimura, The elastic constants of silicon carbide: A Brillouin-scattering
911 study of 4H and 6H SiC single crystals, J. Appl. Phys. 82 (1997) 3152.
912 [36] B.S. Li, C. Zhang, H.P. Liu, L.J. Xu, X. Wang, Z. Yang, F.F. Ge, W.
913 Gao, T.L. Shen, Microstructural and elemental evolution of polycrystalline
914 α-SiC irradiated with ultra-high-fluence helium ions before and after
915 annealing, Fus. Eng. Des. 154 (2020) 111511.
916 [37] Y. Katoh, N. Hashimoto, S. Kondo, L.L. Snead, A. Kohyama,
917 Microstructural development in cubic silicon carbide during irradiation at
918 elevated temperatures, J. Nucl. Materl. 351 (2006) 228–240.
919 [38] C.B. Carter, D.B. Williams, Transmission electron microscopy: a text
920 book for materials science, Springer: New York, 1996.
921 [39] S. Sandlobes, M. Friak, S. Zaefferer, A. Dick, S. Yi, D. Letzig, Z. Pei,
922 L.F. Zhu, J. Neugebauer, D. Raabe, The relation between ductility and
923 stacking fault energies in Mg and Mg–Y alloys, Acta Mater. 60 (2012)
924 3011–3021.
925 [40] H. Zhang, Zhongwen Yao, G. Morin, M. Griffiths, TEM
926 characterization of in-reactor neutron irradiated CANDU spacer material
927 Inconel X-750, J. Nucl. Materl. 451 (2014) 88–96.
928 [41] S. Sandlöbes, M. Friák, J. Neugebauer, D. Raabe, Basal and non-basal
929 dislocation slip in Mg-Y, Mater. Sci. Eng. A 576 (2013) 61–68.

[42] Y. Lin, L. Chen, C. Hsieh, A. Hu, S. Lo, F. Chen, J. Kai, Atomic structure of nano voids in irradiated 3C-SiC, J. Nucl. Materl. 498 (2018) 71–75.

[43] Eiji Okunishi, Hidetaka Sawada, Yukihito Kondo, Experimental study of annular bright field (ABF) imaging using aberration-corrected scanning transmission electron microscopy (STEM), Micron 43 (2012) 538–544.

[44] J. Q. Liu, M. Skowronski, C. Hallin, R. Soderholm, H. Lendenmann, Structure of recombination-induced stacking faults in high-voltage SiC p- n junctions, Appl. Phys. Lett. 80 (2002) 749–751.

[45] A. L. Hannam, P. T. B. Shaffer, Revised X-ray Diffraction Line Intensities for Silicon Carbide Polytypes, J. Appl. Cryst. 2 (1969) 45.

[46] J. Li, Z. Wang, C. Chen, S. Huang, Atomic-scale observation of migration and coalescence of Au nanoclusters on YSZ surface by aberration-corrected STEM, Sci. Rep. 4 (2014) 5521.

[47] K. Watanabe, E. Asano, T. Yamazaki, Y. Kikuchi, I. Hashimoto, Symmetries in BF and HAADF STEM image calculations, Ultramicroscopy 102 (2004) 13–21.

[48] S. J. Pennycook, D. E. Jesson, High-resolution Z-contrast imaging of crystals, Ultramicroscopy 37 (1991) 14–38.

[49] M. Bockstedte, A. Mattausch, O. Pankratov, Ab initio study of the migration of intrinsic defects in 3C-SiC, Phys. Rev. B 68 (2003) 205201.

[50] F. Gao, W. J. Weber, Recovery of close Frenkel pairs produced by low energy recoils in SiC, J. Appl. Phys. 94 (2003) 4348–4356.

953 [51] E. Oliviero, M.F. Beaufort, J.F. Barbot, A. van Veen, A.V. Fedorov,
954 Helium implantation defects in SiC: A thermal helium desorption
955 spectrometry investigation, J. Appl. Phys. 93 (2003) 231–238.
956 [52] Y. W. Zhang, W. J. Weber, Ion irradiation and modification: The role of
957 coupled electronic and nuclear energy dissipation and subsequent
958 nonequilibrium processes in materials, Appl. Phys. Rev. 7 (2020) 041307.
959 [53] G. Velişa, E. Wendler, S. Zhao, et al. Delayed damage accumulation by
960 athermal suppression of defect production in concentrated solid solution
961 alloys, Mater. Res. Lett. 6 (2018) 136–141.
962 [54] M.W.D. Cooper, C.R. Stanek, J.A. et al. Simulation of radiation driven
963 fission gas diffusion in UO2, ThO2and PuO2, J. Nucl. Mater. 481(2016)
964 125.
965 [55] M. Bockstedte, A.r Mattausch, O. Pankratov, Ab initio study of the
966 annealing of vacancies and interstitials in cubic SiC: Vacancy-interstitial
967 recombination and aggregation of carbon interstitials, Phys. Rev. B 69
968 (2004) 235202.
969 [56] P. H. Dederiches, C. Lehmann, H. R. Schober, A. Scholz, R. Zeller,
970 lattice theory of point defects, J. Nucl. Mater. 69-70 (1978) 176-199.
971 [57] J. Li, L. Porter, S. Yip, Atomistic modeling of finite-temperature
972 properties of crystalline b-SiC II. Thermal conductivity and effects of point
973 defects, J. Nucl. Materl. 255 (1998) 139–152.
974 [58] L. Ponsonnet, C. Donnet, K. Varlot, J.M. Martin, A. Grill, V. Patel,
975 EELS analysis of hydrogenated diamond-like carbon films, Thin Solid
976 Films, 319 1998 97–100.

[59] S. Wakeland, R. Martinez, J. K. Grey, C. C. Luhrs, Production of graphene from graphite oxide using urea as expansion–reduction agent, Carbon, 48 (2010) 3463–3470.

[60] P.G. Baranov, I.V. Llyin, A.A. Soltamova, E.N. Mokhov, Identification of the carbon antisite in SiC: EPR of ^{13}C enriched crystals, Phys. Rev. B 77 (2008) 085120.

[61] S. Kondo, A. Kohyama, T. Hinoki, Anisotropic evolution of Frank loops in ion-irradiated silicon carbide, J. Nucl. Materl. 367-370 (2007) 764–768.

[62] W. Jiang, W.J. Weber, Anisotropy of disorder accumulation and recovery in 6H–SiC irradiated with Au^{2+} ions at 140 K, J. Nucl. Materl. 389 (2009) 332–335.

[63] R. W. Harrison, S.Ebert, J. A. Hinks, S.E. Donnelly, Damage microstructure evolution of helium ion irradiated SiC under fusion relevant temperatures, J. Eur. Ceram. Soc. 38 (2018) 3718-3726.

[64] E. Rauls, T.E.M. Staab, Z. Hajnal, Th. Frauenheim, Interstitial-based vacancy annealing in 4H–SiC, Physica B 308–310 (2001) 645–648.

[65] S. Leclerc, M.F. Beaufort, A. Declémy, J.F. Barbot, Strain-induced drift of interstitial atoms in SiC implanted with helium ions at elevated temperature, J. Nucl. Mater. 397 (2010) 132–134.